Evolving flexure recorded in continental rift uplifting landscapes - Corinth Rift, Greece

David Fernández-Blanco[1], Gino de Gelder[1], Sean Gallen[2], Robin Lacassin[1] & Rolando Armijo[1]

[1] Institut de Physique du Globe de Paris, Sorbonne Paris Cité, Univ Paris Diderot, UMR 7154 CNRS, F-75005 Paris, France

[2] Geological Institute, Swiss Federal Institute of Technology (ETH), 8092 Zürich, Switzerland

Abstract

Elastic flexure of the lithosphere is commonly used to model crustal mechanics, rheology and dynamics. However, accurate characterizations of flexure in nature at the spatiotemporal scale of active continental rifting (tens of km; 10^4-10^6 yr) are scant. We use exceptionally preserved geomorphic evidence in the asymmetric, young and fast-extending Corinth Rift, central Greece, to document the combined effect of progressive uplift and footwall flexure throughout its uplifting margin. Across the rift margin, footwall longitudinal river profiles and topography define uplift increasing exponentially towards the bounding fault. Along the rift margin, geomorphic proxies for fault's footwall relief, slip rate and uplift rate show parabolic distributions decaying along strike away from the fault center. Conspicuous drainage reversals where the topographic expression of elastic flexure is most prominent similarly suggest that maximum slip rates occur at the rift center. Overall, the geomorphic evidence for flexure implies disruptive Middle Pleistocene onset of a highly-localized, master fault system of crustal scale controlling the growth of the modern Corinth Rift. Similar highly-localized strain and associated elastic flexure of the lithosphere may have occurred elsewhere, including old and/or slow-extending rifts and areas of intracontinental extension lacking adequate geomorphic evidence.

Keywords: elastic flexure; Corinth Rift; continental rift; footwall uplift; drainage reversal; normal fault

Introduction

Continental regions undergoing extensional faulting often show localized, crustal-scale elastic flexure (Fig. 1A) (e.g., King and Ellis, 1990). In these regions, the up-flexed topography is sustained by isostasy with localized strain in high-angle normal faults across a thick plate (Buck, 1993). Similar flexural strain, albeit of much smaller amplitude, occurs during $M_w \geq 6$ earthquakes in high-angle faults, suggesting that kilometer-scale long-term flexural relief may result from cumulative seismic events (King et al., 1988). By contrast, low-angle faults growing in a thin lithosphere develop little to no elastic flexure (e.g., Forsyth, 1992). Footwall up-warping can thus be used to discern between mechanical modes of continental extension (Bell et al., 2017), and the wavelength and curvature of flexural uplift to model the rheology of the lithosphere (Armijo et al., 1996; de Gelder et al., 2018).

Observations of topography are the principal, yet relatively imprecise, evidence of flexural uplift in large Cenozoic continental rifts, as the East African and Baikal rifts, and in individual grabens within wider areas of diffuse extension, like the Basin and Range and Tibet. There, uplifted rift margins and footwalls have short-wavelength tilts and sporadically steer drainage reversals (Doornkamp and Temple, 1966; Stewart, 1978; Armijo et al., 1986; Petit and Ebinger, 2000). Finer characterisation of flexural uplift is typically precluded by the limited unambiguous geomorphological evidence in relatively old (>10 Ma) extensional regions or restricted to individual transects and/or short temporal scales (up to 10^3 yr) (Thompson and Parsons, 2016).

Here, our main goal is to characterize the spatiotemporal evolution of elastic flexure during intracontinental extension. We study the uplifting, southern margin of the young and rapidly extending continental rift of Corinth (Fig. 1B), where a well-preserved set of late Pleistocene marine terraces and recently inverted large river catchments record flexural uplift on timescales of 10^4-10^6 yr (Fig. 1C) (Armijo et al., 1996; de Gelder et al., 2018). We use a 20m-resolution digital elevation model to (i) analyse longitudinal profiles of river catchments orthogonal to the fault strike; (ii) portray the landscape topography of the rift margin; and (ii) examine geomorphic proxies for uplift near the fault. By these means, we assess the finite geometry of the footwall flexural uplift throughout

the rift margin, characterizing the pattern of elastic flexure. This allows us to discern a disruptive rift growth process in Corinth that can be generalized elsewhere to continental rifts of any age or extension rate.

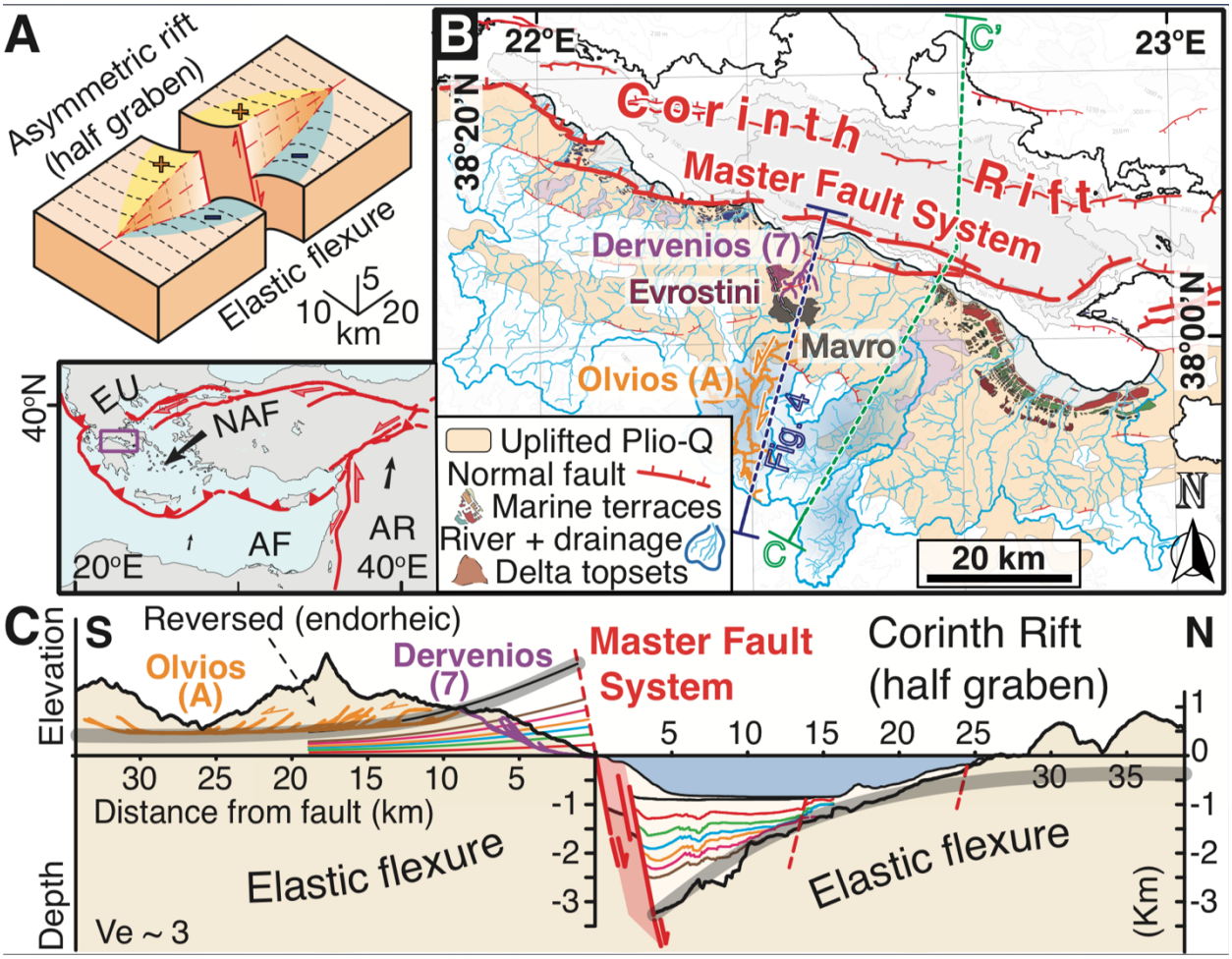

Fig. 1. (A) Block diagram with flexural uplift and subsidence expected for a steep planar master fault. (B) Corinth Rift active tectonics map, showing the approximate location of section in C and Fig. 3. Endorheic drainages are blue shaded. (C) Onshore-offshore cross-section across rift, with projected paleohorizons and river profiles, showing elastic flexure (modified after de Gelder et al., 2018). Correlatable paleohorizons are shown in different colors for up-flexed terraces in fault footwall and down-flexed seismic horizons in fault hanging-wall. Olvios reversed river profile flowing south to the headwaters, and its former downstream reach, the Dervenios river, flowing to the gulf are shown in orange and purple.

Corinth Rift key observations

The main fault system bounding the Corinth Rift sustains the highest seismicity in continental Europe and accommodates faster strain rates (~1-1.5 cm×yr^{-1}) (e.g., Avallone et al., 2004; Bernard et al., 2006) of any subaerially-exposed normal fault on Earth (Charalampakis et al., 2014). This extensional fault system, which dips north and sets the rift marked asymmetry for ~130 km along its southern margin (Fig. 1), has rates of footwall uplift exceeding ~1 mm/yr for the last ~330 ky (e.g., Armijo et al., 1996; McNeill and Collier, 2004).

In the rift center, windgaps carved in south-tilted Middle Pleistocene conglomerates of deltaic systems set the boundary between formerly connected drainages; steep and short beheaded catchments drain toward the gulf, northward of large reversed drainages that now infill flat sedimentary plains with a gentle tilt south (Fig. 1B, C) (Dufaure, 1977; Seger and Alexander, 1993). The uppermost abandoned valley, carved the oldest delta (Mavro), aligns with the windgap of a younger delta (Evrostini), located northwestward at lower elevations (Fig. 1B), implying that the same river bypassed the former to feed the latter, which chrono- and lithostratigraphical correlations suggest deposited by ~0.7 Ma (Ford et al., 2016).

Similar sequences of offlapping stranded deltas becoming younger coastward occur across the rift margin (Fig. 1B) (Seger and Alexander, 1993). This, and former hanging-wall sediments uplifted by sequentially younger footwalls, suggest basinward migration of border fault systems (e.g., Gawthorpe et al., 2017). An extensive flight of marine terraces preserved in the eastern footwall (Armijo et al., 1996), and prominent syntectonic sedimentary wedges of correlatable seismic units in the hanging-wall (Nixon et al., 2016) record an exponential increase in elastic flexure amplitude toward the present rift bounding fault (Fig. 1C) (de Gelder et al., 2018). Markers show the growth of >5 km of structural relief since onset of faulting in the active fault (Fig. 1C), which localized strain developed the current rift asymmetry in a ~300 kyr interval (Nixon et al., 2016). This younger rift phase, discriminating an early proto-Gulf from a modern Corinth Rift (Ori, 1989), is explained by

either progressive rift localization along bounding faults (Ford et al., 2016; Gawthorpe et al., 2017) or by disruptive growth of a high-angle fault <1Ma (Armijo et al., 1996).

Results: Footwall topography and rivers

Footwall river catchments and topography reflect the long-term distribution of footwall uplift controlling rift margin growth, ultimately defined by slip on active normal fault(s). Morphometric analyses that attempt to resolve uplift signals using drainage basin-scale metrics (Demoulin et al., 2015), however, are not suited for cases of flexure, since they average the spatially varying strike-perpendicular component of uplift across catchment. To avoid potential complications, we design our study to resolve the across and along components of flexural uplift with analyses grounded in normal fault mechanics (e.g., Cowie and Scholz, 1992; Cowie et al., 2006). We analyze footwall river profiles and topography in the rift margin sector where the bounding fault strikes continuously for ~60 km (Fig. 2A). This "main" sector includes 11 of the 16 largest rivers catchments draining north, almost orthogonally toward the master fault, and the 3 catchments with reversed drainage, now mostly flowing inland toward their former headwaters (Fig. 2A). See details about the data, topographic and fluvial metrics used in the Data Repository.

The profile morphology and geometry of fault-orthogonal footwall river catchments, oriented as to experience the maximum gradient in footwall flexural uplift, departure from theoretical equilibrium, i.e. smooth-graded, concave-upward profiles (Fig. 1C, 2B). All river profiles exhibit a principal inflection, defined as either a convex-up knickpoint zone or a windgap, marking a stark morphologic transition at ~15-25 km from the active fault (Fig. 2B). This principal inflection separates either steep lower reaches from broad, low gradient uplands reaches with different degrees of back-tilt along fault strike or gulf draining rivers from endorheic basins that record inversion (Figs. 1, 2). Given that most rivers steepen in response to enhanced rates of rock uplift

(Snyder et al., 2000), we infer that the large knickpoints and windgaps are of common origin, resulting from a rapid increase in uplift rate along the full length of the master fault system.

To characterize the long-term activity of the bounding fault along the main rift sector, we analyze both footwall topography, using swath topographic profiles stacked orthogonally to the master fault, and fault footwall relief, approximated by the vertical local elevation change from the active fault to the first major topographic break of slope (Whittaker and Walker, 2015). Stacked-swath profiles show a sharp transition from a steep coastal topography up to ~1.5 km in elevation at ~15 km from the fault into a flat topography sloping southward <300 m in horizontal distances of ~30 km (Fig. 2C). This across-margin footwall topography is self-consistent along the main sector strike (~60 km) and accordant with the flexural uplift signal derived from marine terraces located immediately eastward (Fig. 1C, 2C) (de Gelder et al., 2018). The gradient of fault footwall relief along the same sector shows an asymmetric parabola decaying from its center (Fig. 2D). Hence, the general topography is consistent with a signal of elastic footwall flexure at the scale of the rift margin resulting from parabolic displacement along a single composite master fault system.

We use the longitudinal profiles of river trunks to derive the along-fault distribution in the elevations of principal inflections (knickpoints and windgaps) and the values of normalized steepness index (k_{sn}) below each inflection (Fig. 2D, E). The former depends on the relative along-strike throw rate increase on the driving fault (e.g., Whittaker and Walker, 2015), and the latter is sensitive to the rock uplift rate (Snyder et al., 2000). We use these metrics as proxies for the magnitude of along-strike footwall uplift and uplift rate, respectively, and ultimately relate them with the along-strike distribution of slip and slip rate of the master fault. The elevation of the principal inflection is the highest in the center of the modern rift and decays systematically along rift margin strike (Fig. 2D). Similarly, the lateral gradients in k_{sn} of the downstream reaches portray a parabolic decay from rift center (Fig. 2E). We interpret the lager k_{sn} values in the Vouraikos River (3) as the result of recent fault linkage. The distribution of footwall metrics sensitive to relative uplift rates

record along-strike variations in flexural uplift that also appear consistent with slip along a single, composite master fault system acting at the rift margin scale.

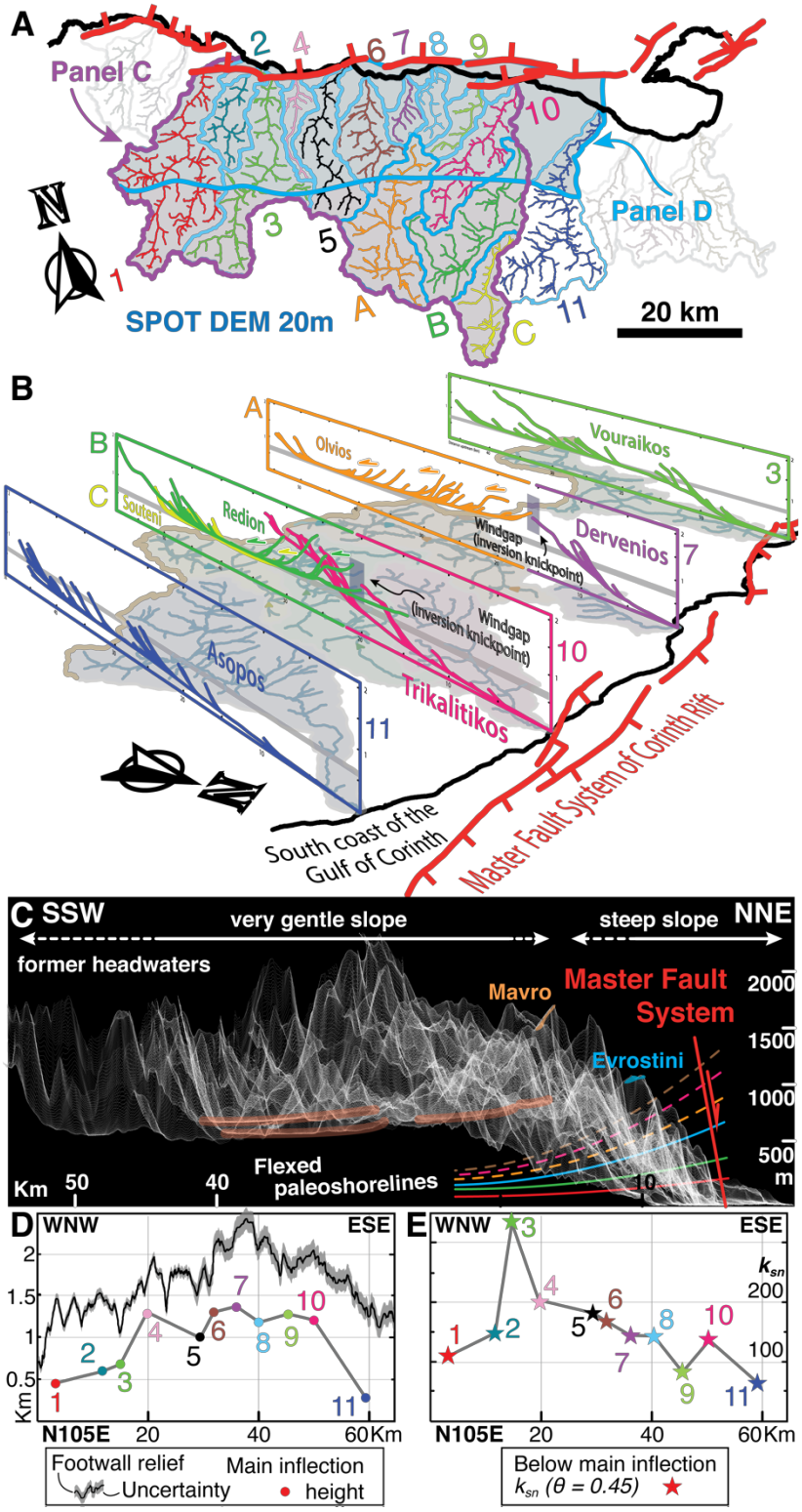

Fig. 2. (A) Index map, with indication of "main" sector DEM area used for C and D. (B) 3D view of river catchment longitudinal profiles and their drainages with regards to the master fault system. Note the prominent size of the inverted catchments in the center of the rift. (C) View of topography along ~60 km of the south rift flank, exaggerated vertically ~8 times, resulting from projecting 300 swath profiles perpendicular to the master fault strike. Distribution along master fault strike of (D) footwall relief and height of the main inflection and (E) normalized steepness index (k_{sn}) of river reaches below each inflection. Footwall relief is the height difference between the principal inflection and the master fault trace, measured vertically. Uncertainty is estimated from fault mapping precision, and the relative departure between fault strike and projection strike.

River location relative to active fault trace and recent drainage reversals hinder a finer along-strike finite characterisation of flexure. Larger uncertainties exist as the fault diverges from river outlet east of river 6 (Fig. 2A, D). Similarly, we expect larger k_{sn} values for equilibrated river catchments that recently lost drainage area (beheaded rivers 6 to 10, Fig. 2A, E). Thus, while the along-strike parabolic distributions (Fig. 2D, E) are consistent with maximum cumulative footwall flexural uplift and uplift rate in the rift center, we attribute larger confidence to the finite geometry of the western half of the parabola.

Discussion

Geomorphic evidence along most of the southern margin of the Corinth Rift characterizes elastic flexure at rift scale associated with its active fault. Footwall river profiles and topography suggest an across strike pattern of footwall uplift that increases exponentially in amplitude toward the bounding fault (Fig. 2B, C). The along strike pattern of footwall relief, inflection point elevation and k_{sn} are best described by a parabolic pattern of cumulative uplift and uplift rate along fault strike (Fig. 2D, E). Collectively, these observations suggests that the modern rift active fault system (Fig. 1B, C) conforms a single, kinematically-linked master fault that imposes a mechanical flexure over the entire southern margin of the Corinth Rift (Fig. 1A).

We infer fast uplift and slip rates all along the Corinth Rift master fault. Footwall river profiles in the rift margin record the along-strike variation associated with flexural uplift of the footwall and the corresponding variations in slip rate at the master fault. Larger increases in footwall uplift rate result in higher elevations of the principal river profile inflections (Fig. 2B, D). This suggests normal fault flexural uplift caused river profiles to adjust by steepening their lower reaches and forcing a marked, differential along-strike, back-tilt in their upper reaches. Beheaded drainages in the central part of the rift, where we infer the most rapid uplift, indicate flexural uplift rates exceed the river

incision rates and resulted in drainage reversal of upper reaches, an inference supported by numerical models (Cowie et al., 2006).

Our results support the highly-localized, disruptive growth of the modern Corinth Rift master fault since its onset. The along-strike remarkable consistency of cumulative elastic flexure signal observed in the topography (Fig. 2C) and its coherency with the shorter-term flexure signal marked by Pleistocene marine terraces (Armijo et al. 1996) suggest highly-localized strain in the master fault since its onset. Disruptive fault onset and growth leading to fast evolution of the modern rift margin is supported by the morphological similarity between footwall river profiles and topography (cf. Fig. 2B,C), as well as by proto-Gulf infill rocks now uplifted in the footwall, which effectively function as passive markers of growth in the high-relief, modern Corinth Rift (Fig. 3) (Ori 1989; Armijo et al. 1996). This agrees with modeling studies suggesting that large-scale flexural footwall uplift requires coseismic slip in localized high-angle faults that reach at least the brittle-ductile transition (Bell et al. 2017; de Gelder et al. 2018) and an isostatic elastic response of the whole crust (e.g., King and Ellis, 1990).

We propose a conceptual model compatible with the rapid, disruptive development of a single crustal fault that is consistent with geologic observations in the central part of the Corinth Rift (Fig. 3). The model illustrates the progressive step-by-step abandonment of Gilbert fan delta sequences and river drainage reversals as direct outcomes of rapidly increasing footwall flexural uplift as normal slip increases across the master fault (Fig. 3). The model suggests that the onset of the present-day master fault, and thus the change in tectonic boundary conditions, postdates deposition in Mavro Delta, and predates deposition in Evrostini delta (Fig. 1B, 2C, 3), which Ford et al. (2016) sets at ~0.7 Ma. Subsequent margin flexural uplift forced abandonment of the Evrostini Delta and disconnected the upper reaches of its feeding catchment. The development of the rift asymmetry during a ~300 ky interval, inferred to start at ~620 ka (Nixon et al., 2016), agrees with our evidence and interpretation supporting the fast, disruptive growth along strike of the master

fault. We thus infer that the master fault controls the growth of the modern Corinth Rift. Therefore, while the older (>1 Ma), distributed extension in the area may well be explained by basinward fault migration (e.g., Gawthorpe et al., 2017), the evidence presented here for elastic flexure throughout the southern margin of the modern Corinth Rift indicates the sudden onset of a Middle Pleistocene rift-forming fault system (Armijo et al., 1996).

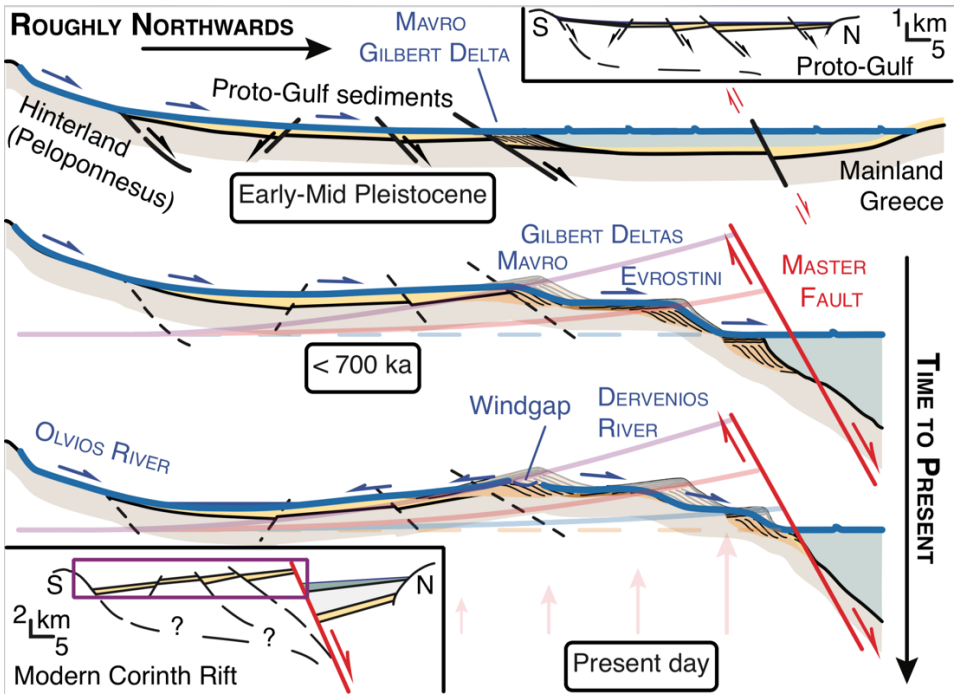

Fig. 3. Conceptual time-evolution of river profiles and Gilbert deltas in the center of the rift (location in Fig. 1B) in relation to elastic flexure of the rift footwall. Not to scale. Footwall flexural uplift is marked in dimmed colors. Upper and bottom profiles represent the Early-Mid Pleistocene and Present-day, respectively, and the time-step in-between can be broadly assigned to <700 ka. Drainage reversal could have taken place any time thereafter, although only shown for the last time-step (see main text). Insets show overarching basinal architecture for the proto-Gulf (upper right) and the Modern Corinth Rift (lower left).

Our work illustrates that the evolving elastic flexure associated with regional-scale faults (tens of km) during long-term (10^4-10^6 yr) extension of continental lithosphere is recorded in their uplifting landscapes. Our analysis, when used alongside privileged geomorphic evidence, reveal the evolving, combined the effect of progressive footwall flexure and uplift. Evolving elastic flexural uplift result in different degrees of landward tilting and drainage reversals in the upstream reaches of the

river catchment. River catchment reversals observed in older and/or low-extending rifts and individual grabens (Doornkamp and Temple, 1966; Stewart, 1978; Armijo et al., 1986; Petit and Ebinger, 2000) suggest that similar flexural uplift and highly-localized strain may occur as intrinsic processes of intracontinental extension, masked by denudation or unambiguous geomorphological evidence. The generalization of elastic flexure processes to intracontinental extension areas of any age or extension rate implies that the process of rifting is highly localized in strain, and disruptive in space and possibly in time.

Acknowledgements

We thank Patience Cowie for detailed comments and discussion of an earlier version of the manuscript. The research leading to these study has received funding from the People Programme (Marie Curie Actions) of the European Union's Seventh Framework Programme under the ITN project ALErT (Grant FP7-PEOPLE-2013-ITN number 607996) and by the ISIS program of CNES.

References

Armijo, R., Meyer, B., King, G.C.P., Rigo, A., and Papanastassiou, D., 1996, Quaternary evolution of the Corinth Rift and its implications for the Late Cenozoic evolution of the Aegean: Geophysical Journal International, v. 126, p. 11–53.

Armijo, R., Tapponnier, P., Mercier, J.L., and Han, T.-L., 1986, Quaternary extension in southern Tibet: Field observations and tectonic implications: Journal of Geophysical Research, v. 91, p. 13803–13872.

Avallone, A., Briole, P., Agatza-Balodimou, A.M., Billiris, H., Charade, O., Mitsakaki, C., Nercessian, A., Papazissi, K., Paradissis, D., and Veis, G., 2004, Analysis of eleven years of deformation measured by GPS in the Corinth Rift Laboratory area: Comptes Rendus: Geoscience, v. 336, p. 301–311.

Bell, R.E., Duclaux, G., Nixon, C.W., Gawthorpe, R.L., and McNeill, L.C., 2017, High-angle, not low-angle, normal faults dominate early rift extension in the Corinth Rift, central Greece: Geology, doi: 10.1130/G39560.1.

Bernard, P., Lyon-Caen, H., Briole, P., Deschamps, A., Boudin, F., Makropoulos, K., Papadimitriou, P., Lemeille, F., Patau, G., Billiris, H., Paradissis, D., Papazissi, K., Castarède, H., Charade, O., et al., 2006, Seismicity, deformation and seismic hazard in the western rift of Corinth: New insights from the Corinth Rift Laboratory (CRL): Tectonophysics, v. 426, p. 7–30.

Buck, W.R., 1993, Effect of lithospheric thickness on the formation of high- and low-angle normal faults: Geology, v. 21, p. 933–936.

Charalampakis, M., Lykousis, V., Sakellariou, D., Papatheodorou, G., and Ferentinos, G., 2014, The tectono-sedimentary evolution of the Lechaion Gulf, the south eastern branch of the Corinth graben, Greece: Marine Geology, v. 351, p. 58–75.

Cowie, P.A., Attal, M., Tucker, G.E., Whittaker, A.C., Naylor, M., Ganas, A., and Roberts, G.P., 2006, Investigating the surface process response to fault interaction and linkage using a numerical modelling approach: Basin Research, v. 18, p. 231–266.

Cowie, P.A., and Scholz, C.H., 1992, Displacement-length scaling relationship for faults: data synthesis and discussion: Journal of Structural Geology, v. 14, p. 1149–1156.

Demoulin, A., Beckers, A., and Hubert-Ferrari, A., 2015, Patterns of Quaternary uplift of the Corinth rift southern border (N Peloponnese, Greece) revealed by fluvial landscape morphometry: Geomorphology, v. 246, p. 188–204.

Doornkamp, J.C., and Temple, P.H., 1966, Surface, Drainage and Tectonic Instability in Part of Southern Uganda: The Geographical Journal, v. 132, p. 238–252.

Dufaure, J.-J., 1977, Néotectonique et morphogenèse dans une péninsule méditerranéenne: Le Péloponnèse: Revue de géographie physique et de géologie dynamique, v. 19, p. 27–58.

Ford, M., Hemelsdaël, R., Mancini, M., and Palyvos, N., 2016, Rift migration and lateral propagation: evolution of normal faults and sediment-routing systems of the western Corinth rift (Greece): Geological Society, London, Special Publications, v. 439, doi: 10.1144/SP439.15.

Forsyth, D.W., 1992, Finite extension and low-angle normal faulting: Geology, v. 20, p. 27–30.

Gawthorpe, R.L., Leeder, M., Kranis, H., Skourtsos, E., Andrews, J., Henstra, G., Mack, G., Muravchik, M., Turner, J., and Stamatakis, M., 2017, Tectono-sedimentary evolution of the Plio-Pleistocene Corinth rift, Greece: Basin Research, doi: 10.1111/bre.12260 .

de Gelder, G., Fernández-Blanco, D., Melnick, D., Duclaux, G., Bell, R., Jara-Muñoz, J., Armijo, R., and Lacassin, R., 2018, Fault flexure and lithosphere rheology set from climate cycles record in the Corinth Rift:, Earth ArXiv preprint doi: 10.17605/OSF.IO/4SH8E.

King, G., and Ellis, M., 1990, The origin of large local uplift in extensional regions: Nature, v. 348, p. 689–693.

King, G.C.P., Stein, R.S., and Rundle, J.B., 1988, The Growth of Geological Structures by Repeated Earthquakes 1. Conceptual Framework: Journal of Geophysical Research, v. 93, p. 13307–13318.

McNeill, L.C., and Collier, R.E.L., 2004, Uplift and slip rates of the eastern Eliki fault segment, Gulf of Corinth, Greece, inferred from Holocene and Pleistocene terraces: Journal of the Geological Society, v. 161, p. 81–92.

Nixon, C.W., McNeill, L.C., Bull, J.M., Bell, R.E., Gawthorpe, R.L., Henstock, T.J., Christodoulou, D., Ford, M., Taylor, B., Sakellariou, D., Ferentinos, G., Papatheodorou, G., Leeder, M.R., Collier, R.E.L.I., et al., 2016, Rapid spatiotemporal variations in rift structure during development of the Corinth Rift, central Greece: Tectonics, v. 35, doi: 10.1002/2015TC004026.

Ori, G.G., 1989, Geologic history of the extensional basin of the Gulf of Corinth (?Miocene-Pleistocene), Greece: Geology, v. 17, p. 918–921.

Petit, C., and Ebinger, C., 2000, Flexure and mechanical behavior of cratonic lithosphere: Gravity models of the East African and Baikal rifts: Journal of Geophysical Research, v. 105, p. 19151–19162.

Seger, M., and Alexander, J., 1993, Distribution of Plio-Pleistocene and Modern coarse-grained deltas south of the Gulf of Corinth, Greece: Tectonic controls and signatures in sedimentary successions, v. 20, p. 37–48.

Snyder, N.P., Whipple, K.X., Tucker, G.E., and Merritts, D.J., 2000, Landscape response to tectonic forcing: Digital elevation model analysis of stream profiles in the Mendocino triple junction region, northern

California: GSA Bulletin, v. 112, p. 1250–1263.

Stewart, J.H., 1978, 1: Basin-range structure in western North America: A review: Geological Society of America Memoirs, v. 152, p. 1–32.

Thompson, G.A., and Parsons, T., 2016, Vertical deformation associated with normal fault systems evolved over coseismic, postseismic, and multiseismic periods: Journal of Geophysical Research, Solid Earth, v. 121, p. 2153–2173.

Whittaker, A.C., and Walker, A.S., 2015, Geomorphic constraints on fault throw rates and linkage times: Examples from the Northern Gulf of Evia, Greece: Journal of Geophysical Research: Earth Surface, v. 120, doi: 10.1002/2014JF003318.

DATA REPOSITORY

Digital Elevation Models (DEMs). We used the available 30-m horizontal resolution ALOS AW3D30 DSM (ALOS) and patched voids and gaps with ASTER GDEM V2 (ASTER) for an area inclusive of the whole Peloponnese and both margins of the Gulf of Corinth. We upsampled the merged DEM for latitudes north of Nafplion with a 20-m horizontal (post-spacing) resolution SPOT5 DEM of an area that covers the majority of the southern shoulder of the Gulf of Corinth, the Perachora Peninsula and the Kaparelli area. We then clipped the composite DEM using drainage areas of Peloponnesian rivers discharging into the gulf and the three largest reversed rivers that are now endorheic basins, i.e. Feneos, Stymfalia and Skotini. These areas with internal drainage were manually delineated to avoid the inaccuracies of automatic methods.

Staked swaths. Staked swaths (or wide swath) can be used to highlight the coherence of topography and thus the continuity of morphological features in depth over large scales (Armijo et al., 2015). We use stacked swaths to portray the rift margin footwall topography, which we considered extends southwards to include the three largest reversed river catchments, for ~60 km along rift margin strike (Fig. 2B). We use 300 parallel swaths profiles derived from our DEM and stack them together orthogonally to their trends. These swath profiles are perpendicular to the average strike of the active master fault system (taken as N105°E) and are plotted as hairlines in Fig. 2B looking SSW. Swath width is defined dynamically by dividing DEM width along the projection direction by the number of swath profiles, and we estimate the along-fault width of each swath profile to be ~200 m.

Footwall relief. The mountain front relief of an uplifting footwall of an extensional fault system results from long-term uplift rate, and thus slip rate, of its bounding fault. Range front relief results from cumulative fault displacement and can be used to infer the dimensions of the active fault and its history of growth and linkage (e.g., Dawers and Anders, 1995; Gupta and Scholz, 2000). We use an equivalent to range front relief, footwall relief. We define and calculate the along-strike distribution of footwall relief in a similar fashion to Whittaker and Walker (2015). We consider footwall relief as the absolute difference in elevation, measured vertically, from the trace of the fault to the first prominent topographic break in slope in the footwall topography, which represents the crest of frontal relief set by the main triangular facets in the footwall. The first topographic break of slope is observed in the footwall topography near the fault at distances of <20km, often ~15km, measured inland perpendicularly from the fault trace strike. As such, we visually defined

a polygon extending inland for ~21km perpendicular to the fault strike at each fault sector, i.e. an area that clearly covers the inflection (see Fig. 2A). Definition of such polygon removes topography farther away from the fault to facilitate recognition of the first break of slope in the footwall topography. We use this polygon along the "main" sector to calculate ~20m-wide swaths each 20m, with orientations that are perpendicular to the fault trace strike. We use these swaths to derive the position of the first break of slope in the footwall topography, measured vertically from the fault trace, and project it along fault strike, taken as N105E. We graphically attach an estimated uncertainty (Fig. 2D) derived from two factors: confidence in accurate mapping of the fault and discrepancy between fault strike and chosen direction of projection. The master fault can be confidently mapped in the west of the main sector (see Fig. 2A) and uncertainties associated to the position of the fault trace are minimal. However, the position of the master fault is more imprecise eastwards, as the fault lays underwater and its trace cannot be mapped with confidence. As such, we estimate a maximum uncertainty of ~250 m for the eastern main sector due to this effect in combination with the unconstrained growth behavior of the footwall relief underwater. We further attribute a maximum estimated uncertainty of ±50 m to the discrepancy between our chosen projection plane and the fault strike towards the eastern areas of the main sector. We consider the equivalent uncertainty negligible in the western areas of the main sector.

Longitudinal river profiles. First order clues on the evolution of normal fault systems can be deduced from local convexities (knickpoints zones) in the longitudinal profiles of footwall rivers. For example, a change in rock uplift rate will lead to the upstream migration of a knickpoint as a kinematic-wave, and the river channel will steepen in the wake of the passing knickpoint (Rosenbloom and Anderson, 1994). The knickpoint acts as a mobile boundary between a former portion of the stream unaware of a change in uplift rate and an adjusted or adjusting downstream reach (e.g., Whipple and Tucker, 1999; Snyder et al., 2000). We used Topotoolbox 2.0 (Schwanghart and Scherler, 2014) to extract the river profiles and χ Profiler river profile analysis package (Gallen and Wegmann, 2017) for analysis. Fluvial channels were defined as areas draining $\geq 10^6$ m^2 and smoothed with a 500 m moving window average.

To portray river network morphology and the longitudinal profiles of the three reversed, endorheic river catchments, which flow do not reach the regional base level, we performed specific corrections. We set an artificial outlet by creating a sink at the lowest point of the longest stream, and clipped the DEM in the drainage areas north and south of it. We performed stream

flow direction and other suitable procedures as for the rest of the rivers. We oriented the outcome of the longitudinal river profiles according to their general flow direction, i.e. one flowing northwards and one southwards. The resulting longitudinal profile was oriented to match the flow direction in the longitudinal profiles of exorheic rivers.

Height of the main inflections. River profile inflections have vertical rates of propagation that are a function of the change in the rate of footwall uplift (Wobus et al., 2006; Crosby and Whipple, 2006; Attal et al., 2008; Whittaker et al., 2008). Provided uniform climate and substrate properties, knickpoints resulting from a temporal change in uplift rate will propagate vertically at the same rate (Niemann et al., 2001). Along normal faults, which typically show variable rates of uplift along strike, the relative height of knickpoints is a function of this differential along-strike uplift (e.g., higher knickpoints suggest faster fault throw rates) (Whittaker et al., 2008; Whittaker and Walker, 2015). We derive the height of the principal inflection of river catchments flowing towards the hanging-wall, and including both, the height of main knickpoints of trunks longitudinal profiles for rivers flowing towards the gulf, and the height of the windgaps, approximated by the highest point of the behaved rivers.

Normalized steepness index (k_{sn}) below the principal inflections. Researchers have demonstrated that there is a functional relationship between rock uplift rate or erosion rate and river channel steepness normalized upstream by contributing drainage area, which suggests that river channel steepness can be used as a proxy for relative rate of uplift or erosion (Snyder et al., 2000; Ouimet et al., 2009; DiBiase et al., 2010; Gallen and Wegmann, 2017). These empirical studies are supported by quasi-physical models of river incision that imply that bedrock river incision is related to upstream drainage area, a proxy for discharge, and local channel slope (Howard, 1994; Whipple and Tucker, 1999; Tucker and Whipple, 2002). The most general of these models is the detachment-limited stream power incision model, which, when combined with mass-conservation, describes the change in river bed elevation over time as follows,

$$\frac{dz}{dt} = U - E = U - KA^m S^n \quad (1)$$

where *dz/dt* is the change in elevation of the channel bed with time, U is rock uplift rate relative to a fixed base level, E is river erosion, A is the upstream drainage area, S is local channel slope, K

is a dimensional coefficient that incorporates variables dependent on incision process, substrate, climate and hydrology of erosion (e.g., Whipple, 2004), and m and n are positive constants that depend on basin hydrology, channel geometry, and erosion processes (Howard, 1994; Whipple, 2004; Whipple and Tucker, 1999). Assuming steady-state conditions where rock uplift rate and erosion rate are equal, local channel slope can be cast as a function as,

$$S = (U/K)^{1/n} A^{-(m/n)} \quad (2)$$

Equation 2 has the same form as Flint's (1974) law, which describes the equilibrium geometry of a longitudinal river profile as a power law function of upstream contributing drainage area through the channel parameters of the steepness index and concavity index. The steepness index is proportional to the ratio of rock uplift to substrate erodibility and the concavity index is equal to the ratio of m to n (Kirby and Whipple, 2001; Snyder et al., 2000).

The river channel concavity, defined as θ or m/n, is theoretically independent of rock uplift rate or erosion rate but will strongly impact the steepness index of the river. In an effort to remove the influence of channel concavity on the steepness index many researchers use a fixed reference concavity index, defined as θ (m/n), to derive a normalized steepness index, k_{sn}. From theory, the concavity index (θ) should vary between ~0.3 to 0.7, and many empirical studies find a value of ~0.45 for most river profiles near equilibrium or graded conditions (Kirby and Whipple, 2012; Snyder et al., 2000; Wobus et al., 2006). Thus, most researchers use a reference concavity of 0.45, as is used in this study, to calculate the normalized steepness index and assess relative patterns of rock uplift in space and time.

Traditionally, k_{sn} is calculated by a linear regression of $log\ S$ and $log\ A$ (Kirby and Whipple, 2012); however, Perron and Royden (2013) recognized that this approach introduces unwanted noise in the data and they propose the integral or χ method of river profile analysis instead. The χ-analysis relies on a transformation of the horizontal coordinate for a river profile, from distance to χ, where χ is an integral quantity with units of length. Separating variables in Eq (2), assuming U and K are spatially invariant, and integrating yields:

$$z(x) = z(x_b) + \left(\frac{U}{K}\right)^{\frac{1}{n}} \int_{x_b}^{x} \frac{dx}{A(x)^{m/n}} \quad (3)$$

Where z is elevation and x_b is base level. The trailing term on the right-hand side of the equation is unitless. Therefore, a reference drainage area A_o is introduced such that:

$$z(x) = z(x_b) + \left(\frac{U}{KA_o^m}\right)^{\frac{1}{n}} \chi \quad (4)$$

Where:

$$\chi = \int_{x_b}^{x} \left(\frac{A_o}{A(x)}\right)^{m/n} \quad (5)$$

Equation 5 is convenient because it has the form of a line where z is the dependent variable, χ is the independent variable, $z(x_b)$ is the y-intercept and $\left(\frac{U}{KA_o^m}\right)^{\frac{1}{n}}$ is the slope. Plots of χ and z are referred to as χ-plots. It is important to recognize that when A_o is assumed to be 1, the slope in a χ-plot is the same as k_{sn}, thus it is best practice to always use an A_o equal to 1 to standardize χ-plots (e.g., Gallen and Wegmann, 2017).

We calculate the values of the k_{sn} of river streams below the main inflection to infer the patterns of relative rock uplift rate associated with the active fault and their variations along fault strike, providing that erodibility and climatic variations are minor with regards to variations in rock uplift (Kirby and Whipple, 2001).

REFERENCES

Armijo, R., Lacassin, R., Coudurier-Curveur, A., and Carrizo, D., 2015, Coupled tectonic evolution of Andean orogeny and global climate: Earth-Science Reviews, v. 143, p. 1–35.

Attal, M., Tucker, G.E., Whittaker, A.C., Cowie, P.A., and Roberts, G.P., 2008, Modeling fluvial incision and transient landscape evolution: Influence of dynamic channel adjustment: Journal of Geophysical Research, v. 113, p. F02010.

Crosby, B.T., and Whipple, K.X., 2006, Knickpoint initiation and distribution within fluvial networks: 236 waterfalls in the Waipaoa River, North Island, New Zealand: Geomorphology, v. 82, p. 16–38.

Dawers, N.H., and Anders, M.H., 1995, Displacement-length scaling and fault linkage: Journal of Structural Geology, v. 17, p. 607–614.

DiBiase, R.A., Whipple, K.X., Heimsath, A.M., and Ouimet, W.B., 2010, Landscape form and millennial erosion rates in the San Gabriel Mountains, CA: Earth and Planetary Science Letters, v. 289, p. 134–144.

Flint, J.J., 1974, Stream gradient as a function of order, magnitude, and discharge: Water Resources Research, v. 10, p. 969–973.

Gallen, S.F., and Wegmann, K.W., 2017, River profile response to normal fault growth and linkage: An example from the Hellenic forearc of south-central Crete, Greece: Earth Surface Dynamics, v. 5, p. 161.

Gupta, A., and Scholz, C.H., 2000, A model of normal fault interaction based on observations and theory: Journal of Structural Geology, v. 22, p. 865–879.

Howard, A.D., 1994, A detachment-limited model of drainage basin evolution: Water Resources Research, v. 30, p. 2261–2285.

Kirby, E., and Whipple, K.X., 2012, Expression of active tectonics in erosional landscapes: Journal of Structural Geology, v. 44, p. 54–75.

Kirby, E., and Whipple, K.X., 2001, Quantifying differential rock-uplift rates via stream profile analysis: Geology, v. 29, p. 415–418.

Niemann, J.D., Gasparini, N.M., Tucker, G.E., and Bras, R.L., 2001, A quantitative evaluation of Playfair's law and its use in testing long-term stream erosion models: Earth Surface Processes and Landforms: The Journal of the British Geomorphological Research Group, v. 26, p. 1317–1332.

Ouimet, W.B., Whipple, K.X., and Granger, D.E., 2009, Beyond threshold hillslopes: Channel adjustment to base-level fall in tectonically active mountain ranges: Geology, v. 37, p. 579–582.

Perron, J.T., and Royden, L., 2013, An integral approach to bedrock river profile analysis: Earth Surface Processes and Landforms, v. 38, p. 570–576.

Rosenbloom, N.A., and Anderson, R.S., 1994, Hillslope and channel evolution in a marine terraced landscape, Santa Cruz, California: Journal of Geophysical Research, v. 99, p. 14013–14029.

Schwanghart, W., and Scherler, D., 2014, TopoToolbox 2 – MATLAB-based software for topographic analysis and modeling in Earth surface sciences: Earth Surface Dynamics, v. 2, p. 1–7.

Snyder, N.P., Whipple, K.X., Tucker, G.E., and Merritts, D.J., 2000, Landscape response to tectonic forcing: Digital elevation model analysis of stream profiles in the Mendocino triple junction region, northern California: GSA Bulletin, v. 112, p. 1250–1263.

Tucker, G.E., and Whipple, K.X., 2002, Topographic outcomes predicted by stream erosion models: Sensitivity analysis and intermodel comparison: Journal of Geophysical Research, v. 107, p. 2179.

Whipple, K.X., 2004, Bedrock rivers and the geomorphology of active orogens: Annual Review of Earth and Planetary Sciences, v. 32, p. 151–185.

Whipple, K.X., and Tucker, G.E., 1999, Dynamics of the stream-power river incision model: Implications for height limits of mountain ranges, landscape response timescales, and research needs: Journal of Geophysical Research: Solid Earth, v. 104, p. 17661–17674.

Whittaker, A.C., Attal, M., Cowie, P.A., Tucker, G.E., and Roberts, G., 2008, Decoding temporal and spatial patterns of fault uplift using transient river long profiles: Geomorphology, v. 100, p. 506–526.

Whittaker, A.C., and Walker, A.S., 2015, Geomorphic constraints on fault throw rates and linkage times: Examples from the Northern Gulf of Evia, Greece: Journal of Geophysical Research: Earth Surface, v. 120, p. 2014JF003318.

Wobus, C., Whipple, K.X., Kirby, E., Snyder, N., Johnson, J., Spyropolou, K., Crosby, B., and Sheehan, D., 2006, Tectonics from topography: Procedures, promise, and pitfalls: Geological Society of America Special Papers, v. 398, p. 55–74.